Linkages between Amplified Quasi-Stationary Waves and Humid Heat Extremes in Northern Hemisphere Midlatitudes

QIYAN LIN[a] AND JIACAN YUAN[a]

[a] Department of Atmospheric and Oceanic Sciences and Institute of Atmospheric Sciences and CMA-FDU Joint Laboratory of Marine Meteorology and Shanghai Institute for Energy and Carbon Neutrality Strategy, Fudan University, Shanghai, China

ABSTRACT: Humid heat extremes, taking account of both temperature and humidity, have adverse impacts on society, particularly on human health. It has been suggested that quasi-stationary waves (QSWs) with anomalously high amplitudes contribute to the occurrence of near-surface precipitation extremes and temperature extremes in the midlatitudes of the Northern Hemisphere. However, little attention has been paid to the linkages between amplified QSWs and humid heat extremes. Using the ERA5 dataset, we identify amplified QSWs of zonal wavenumbers 5–7 (Wave 5–7) in summer months from 1979 to 2020. These amplified QSWs show clear circumglobal wave patterns horizontally and nearly barotropic structure vertically. Linking amplified Wave 5–7 to wet-bulb temperature (WBT) extremes, we find that amplified QSWs preferentially induce prominently prolonged WBT extremes in specific regions: north-central North America for amplified Wave 5; western United States, south-central Asia, and eastern Asia for amplified Wave 6; and western Europe and the Caspian Sea region for amplified Wave 7. Analyses of physical processes indicate that, accompanied by the amplification of Wave 5–7, the changes in horizontal temperature advection, adiabatic heating associated with descending motion, downward solar radiation, moisture transport and moisture flux convergence, and surface latent heat fluxes largely account for the increase in persistence of WBT extremes.

SIGNIFICANCE STATEMENT: In the context of climate change, humid heat extremes exhibit different changes and impacts from high-temperature extremes, but the physical processes that may cause them remain unclear. This study aims to explore the atmospheric dynamic processes leading to the concurrence of humid heat extremes, which may exacerbate the risk from heat stress in today's interconnected world. In specific regions over the Northern Hemisphere midlatitudes, durations of humid heat extremes are found to be elevated simultaneously by amplified quasi-stationary waves. We further identify the physical connections between amplified quasi-stationary waves and humid heat extremes over targeted regions. This would help in better understanding the role of changing atmospheric circulations in the humid heat extremes.

KEYWORDS: Northern Hemisphere; Atmospheric circulation; Stationary waves; Extreme events; Humidity; Temperature

1. Introduction

The intensity and frequency of heat extremes have exhibited a rise at both global and regional scales during recent decades, and are projected to continuously increase as climate warms (Meehl and Tebaldi 2004; Coumou and Rahmstorf 2012; Seneviratne et al. 2021). It has been manifested that heat extremes have devastating impacts on many sectors of society (Oudin Åström et al. 2013; Dunne et al. 2013; Wang et al. 2020; Weilnhammer et al. 2021; Gampe et al. 2021; Shukla et al. 2021). In particular, heat extremes are often associated with increased mortality due to the limited human thermoregulatory capacity (Patz et al. 2005; Mora et al. 2017).

Heat extremes are commonly analyzed by dry-bulb temperature (DBT) alone, including extreme temperature or indices based on temperature (Coumou et al. 2013; Horton et al. 2016; Dosio et al. 2018; Wang et al. 2020; Fischer et al. 2021). However, recent studies have proposed that the effect of humidity should be considered particularly when assessing heat-induced health impact (heat stress) and the risk of heat-relative mortality, because high humidity generally restrains the efficiency of sweating, an important way by which the body core temperature is cooled down in a hot environment (Kovats and Hajat 2008; Mora et al. 2017). The magnitude of some heatwaves has been starkly amplified when adding the effect of humidity, such as the 1995 Chicago heatwave and the 2003 Shanghai heatwave (Russo et al. 2017). Furthermore, through investigating the joint distribution of summertime relative humidity and daily maximum temperature, Yuan et al. (2020) pointed out that heat stress would increase due to the increase of relative humidity even though at a fixed daily maximum temperature. Indeed, atmospheric moisture has shown an overall rise in a warming climate based on observations and models, consistent with the Clausius–Clapeyron relation, which may enhance the probability of occurrence of humid heat extremes (Willett et al. 2007; Coumou and Rahmstorf 2012).

Hence, the great significance of humid heat extremes has been increasingly emphasized. Among wide varieties of integrated temperature–humidity heat indices, wet-bulb temperature (WBT) is an effective metric for humid heat in climate studies with its clear physical interpretation (Raymond et al. 2017; Wang et al. 2019; Monteiro and Caballero 2019; Raymond et al. 2020; Mishra et al. 2020; Wang et al. 2021; Zhang et al. 2021; Rogers et al. 2021). WBT is empirically defined as the equilibrium temperature of an air parcel at constant pressure when it gets saturated by evaporating water into it consuming the enthalpy from the air parcel itself (Li et al. 2020). According to this definition, WBT represents the lowest temperature that human body can be reached by cooling of perspiration. Analyzing WBT calculated based on conserving enthalpy, Zhang et al. (2021) suggested that the projections of tropical extreme WBT under global warming are constrained by atmospheric dynamics and thus show reduced uncertainty range compared to the projections of tropical extreme temperature under the same global warming scenario.

Evaluated by WBT, humid heat extremes are suggested to significantly increase in frequency and intensity during the past decades and in future projections under global warming (Raymond et al. 2020; Wang et al. 2021). WBT extremes show large differences from DBT extremes in climatological characteristics and recent changes (Rogers et al. 2021). Most current research has focused on regional WBT extremes and corresponding synoptic conditions. Raymond et al. (2017) investigated the spatiotemporal patterns and mechanisms of WBT extremes over the contiguous United States. Similarly, Wang et al. (2019) analyzed the climatological and synoptic characteristics of WBT extremes across China. In addition, Monteiro and Caballero (2019) studied the WBT extremes in southern Pakistan, a hot spot with very high WBT values in South Asia. Still, little work concerns the WBT extremes over the entire midlatitudes of Northern Hemisphere (NH), which may occur simultaneously in remote regions, and the corresponding mechanisms at a hemisphere scale.

One important component of atmospheric circulation is quasi-stationary waves (QSWs), Rossby waves with a phase speed close to zero. The QSWs are normally forced by zonal asymmetries in land–sea thermal contrast, topography, atmospheric diabatic heating, and transient eddy fluxes (Wills et al. 2019). Thus they prefer longitudinal phases that typically persist for longer than synoptic time scales (Wills et al. 2019; Kornhuber et al. 2020; Stendel et al. 2021; Luo et al. 2022). It is demonstrated that QSWs, specifically those with anomalously high amplitudes, contribute to the occurrence of weather extremes at the surface (Screen and Simmonds 2014; Coumou et al. 2014; Yuan et al. 2015; Stadtherr et al. 2016; Lee et al. 2017; Yuan et al. 2018; Wolf et al. 2018; Mann et al. 2018; Kornhuber et al. 2020; Xu et al. 2021). Amplified subtropical stationary waves favor precipitation extremes over specific regions through modifying the large-scale moisture transport in both historical observations and future projections (Yuan et al. 2015, 2018). Stadtherr et al. (2016) concluded that precipitation extremes in the Balkans during May 2014 likely related to QSWs with zonal wavenumber 6 through hemispheric wind field analysis. For heat extremes,

Screen and Simmonds (2014) show that months with extreme temperature in the NH midlatitudes are commonly accompanied by significantly magnified QSWs, predominantly for zonal wavenumbers 5–7, whereas months with near-average temperature are often linked to attenuated QSWs. Moreover, some studies suggest that large-amplitude wave patterns within synoptic wavenumber range (zonal wavenumbers 6–8), generated by quasi-resonant amplification, have led to midlatitude synchronization of temperature extremes on monthly time scales (Petoukhov et al. 2013; Coumou et al. 2014; Petoukhov et al. 2016; Kornhuber et al. 2017). Additionally, Kornhuber et al. (2020) reveal that recurrent high-amplitude Rossby wave patterns with zonal wavenumbers 5 and 7 in summer can induce concurrent temperature extremes in specific regions over the NH midlatitudes, where risks to global crop production are raised.

While most studies focus on temperature extremes, little attention is paid to the linkages between amplified QSWs and humid heat extremes. The QSWs are able to alter the circulation, temperature advection, and moisture flux. Further, they potentially contribute to the concurrence of humid heat extremes in different regions. In this study, we will examine the characteristics of humid heat extremes measured by wet-bulb temperature associated with high-amplitude QSWs in the NH midlatitudes and identify key regions. Moreover, we investigate the physical processes how amplified QSWs in multiple zonal wavenumbers induce humid heat extremes over these regions.

The remainder of this paper is organized as follows. Section 2a gives the data used for this study. Definition of wave amplitudes and criteria used to select months of high-amplitude QSWs are introduced in section 2b. Section 2c gives the description of midlatitude extreme index for WBT. The calculation of WBT and the metric of WBT extremes are described in section 2d. Section 2e introduces the procedure of statistical significance tests. In section 3, the spatial structures of high-amplitude QSWs are presented respectively. Section 4 analyzes the impacts of amplified QSWs on WBT extremes. The possible physical processes for how amplified QSWs drive such WBT extremes are explained in section 5. Finally, section 6 summarizes our conclusions and discusses some remaining issues.

2. Data and methods

a. Data

Atmospheric reanalysis data used in this study are from the ERA5 dataset provided by the European Centre for Medium-Range Weather Forecasts (ECMWF) (Hersbach et al. 2020). We obtain the output data at 1° spatial resolution from the ERA5 website, where the available data have been interpolated by a bilinear method from a native grid resolution (about 30 km). The choice of grid resolution has little effect on our results. We employ monthly means of multiple variables including meridional wind, zonal wind, vertical velocity, geopotential height, temperature, and specific humidity (q) on pressure levels, as well as radiation and heat flux at the surface to investigate the long-lasting weather conditions. In addition, daily 2-m dry-bulb temperature (DBT) and wet-bulb

temperature (WBT) are used to define the weather extremes. The daily WBT values are integrated from hourly WBT, which is calculated from hourly 2-m DBT, 2-m dewpoint temperature, and surface pressure (see more details in section 2d) to ensure the WBT obtained from the three variables at the same time step. Then monthly means of DBT and WBT are calculated by averaging daily near-surface DBT and WBT. We focus on the boreal summer, referring to June–August (JJA), for the period 1979–2020.

As this study focuses on how QSWs affect surface extremes, we first remove the global warming signals in monthly near-surface DBT, WBT, and q by subtracting their linear trends per grid point and month of the year, following previous studies (Screen and Simmonds 2014; Coumou et al. 2014; Kornhuber et al. 2020; Xu et al. 2021). Then, monthly anomalies are obtained by removing the climatological mean of the calendar month at each grid point.

b. Wave amplitudes and months of high-amplitude waves

Previous studies indicated that wave trains defined by meridional wind can highlight shorter zonal scales (Branstator 2002; Xu et al. 2019). Therefore, in this study, the amplitudes of QSWs are determined using a fast Fourier transform on monthly-mean 300-hPa meridional wind meridionally averaged over midlatitudes (30°–60°N). Using the fast Fourier transform, the meridional wind can be decomposed into its basic components:

$$\Psi = A \sin(kx - \varphi), \qquad (1)$$

where A, k, x, and φ are amplitude, wavenumber, longitude, and phase, respectively. The phase φ is defined with respect to 180° as a reference longitude here. This latitude band is selected because it covers the climatological location of jet streams and maximum meridional wind at the 300-hPa level in summer (Fig. S1 in the online supplemental material). Here monthly means are used to remove the transient components of Rossby waves and retain the quasi-stationary components (Coumou et al. 2017).

The climatology of intensity for a wavenumber is calculated by averaging the square of its wave amplitude in each summer month of 1979–2020. The climatological intensity of the first 10 zonal wavenumbers, accounting for the overwhelming majority of variance in the NH midlatitude circulation (Screen and Simmonds 2013), is shown in Figs. 1a–c. The intensity of zonal wavenumbers 5–7 (Wave 5–7 hereafter) stands out in each summer month. Among the first 10 wavenumbers, the variances explained by Wave 5–7 are 57.6%, 64.8%, and 63.5% on average in June, July, and August during 1979–2020, respectively. This is consistent with Wang et al. (2013), indicating more pronounced shortwave variability of NH midlatitude circulation in summer than longwave variability. In addition, studies suggest that quasi-stationary waves are highly relevant to midlatitude weather extremes, predominantly for zonal wavenumbers 5–7 (Screen and Simmonds 2014; Stadtherr et al. 2016; Kornhuber et al. 2020). Thus, we focus on Wave 5–7 in this study.

For each wavenumber in Wave 5–7, the months characterized by high-amplitude QSWs are selected according to two criteria: 1) For a particular wavenumber, months when the wave amplitude exceeds its mean plus standard deviation across all the summer months of 1979–2020 are selected. 2) Among these selected months, we exclude the months when the wave amplitude at this wavenumber is less than either wave amplitude at the other two wavenumbers in the same month. The remaining months are regarded as the high-amplitude wave months for this wavenumber. Based on these two criteria, we have obtained $N = 18$, 17, and 15 months (approximately 14.3%, 13.5%, and 11.9% of cases) when the wave is amplified for wavenumbers 5, 6, and 7, respectively (marked by circles in Figs. 1d–f).

c. Midlatitude extreme index

To quantify concurrence of WBT extremes over the 30°–60°N latitudinal band, we calculate the midlatitude extreme (MEX) index following Coumou et al. (2014):

$$\mathrm{MEX}(x,t) = \frac{\frac{1}{N}\sum_{i}^{N}\left[\frac{\Delta x_i(t)}{\sigma(x_i)}\right]^2 - \mu_{\mathrm{MEX}}}{\sigma_{\mathrm{MEX}}}, \qquad (2)$$

where x denotes monthly WBT consisting of N grid points only on land throughout the midlatitudes; $\Delta x_i(t)$ is the anomaly of x derived by removing linear trend and seasonal cycle and $\sigma(x_i)$ is the standard deviation of Δx, in which t refers to the time step and i refers to the grid point. Then the MEX is normalized by subtracting its mean (μ_{MEX}) and dividing by its standard deviation (σ_{MEX}). High positive MEX values indicate WBT extremes occurring simultaneously in many locations throughout the targeted latitudinal band.

d. WBT calculation and metric of WBT extremes

We use wet-bulb temperature to measure humid heat. First, we convert 2-m dewpoint temperature (T_d; unit: °C) and surface pressure (p_s; unit: Pa) to near-surface specific humidity (q; unit: kg kg^{-1}) using the following approximation:

$$e = 611.2 \exp\left(\frac{17.67 T_d}{T_d + 243.5}\right), \qquad (3)$$

$$q = \frac{0.622}{p_s - 0.378 e}. \qquad (4)$$

Then following Li et al. (2020), WBT is calculated by numerically solving the equation based on conserving enthalpy:

$$c_p \mathrm{DBT} + Lq = c_p \mathrm{WBT} + \epsilon L e_s(\mathrm{WBT})/p_s, \qquad (5)$$

where DBT, q, and p_s are near-surface dry-bulb temperature, near-surface specific humidity and surface pressure, respectively; c_p denotes the specific heat capacity of air at constant pressure; ϵ is the molecular mass ratio of water vapor and air; e_s is the saturation vapor pressure; L is the latent heat of
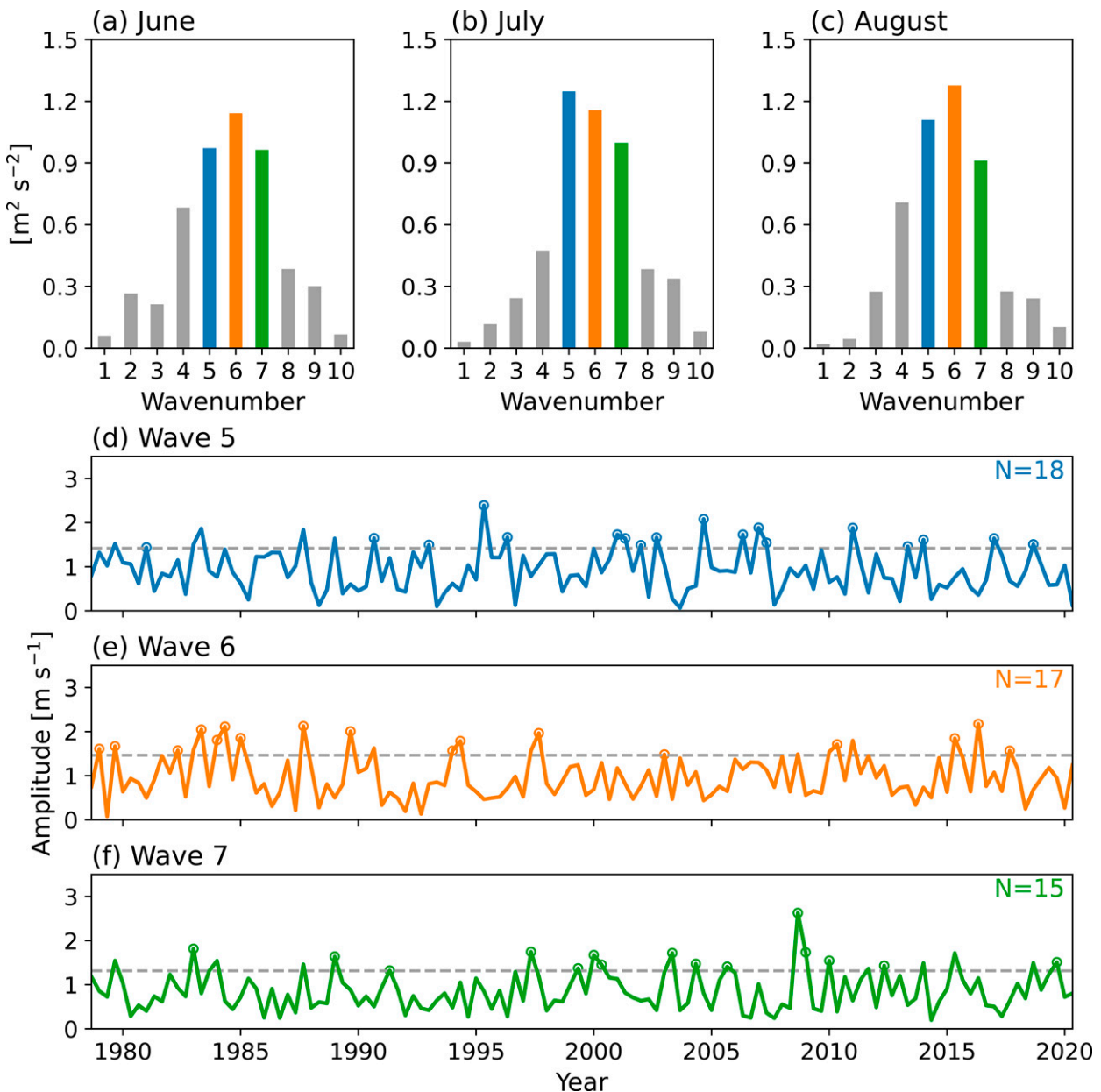
FIG. 1. Climatological intensity of the first 10 zonal wavenumbers in (a) June, (b) July, and (c) August of 1979–2020. Time series of amplitudes for (d) Wave 5, (e) Wave 6, and (f) Wave 7 in months of 1979–2020 summer, respectively. Gray dashed lines denote mean plus one standard deviation and circles denote months of high-amplitude waves. The numbers of months of high-amplitude Wave 5–7 are respectively labeled at the top right of (d)–(f).

condensation; and e_s(WBT) is saturation vapor pressure at temperature WBT, which is obtained from the Clausius-Clapeyron relation.

To measure WBT extremes, we use a metric named extreme humid heat maximum duration (EHHMDur). We first define extreme humid heat day as a day on which the daily maximum WBT exceeds the 95th percentile of daily maximum WBT distribution over JJA of 1979–2020. Prior to calculating the thresholds, we remove the linear trend and calendar-day mean at each grid point to eliminate the influences from long-term

trend and seasonal cycle. From this definition, EHHMDur refers to the number of maximum consecutive extreme humid heat days within a month. For comparison, we also calculate extreme high temperature maximum duration (EHTMDur) in a similar way to measure high-temperature extremes, which are produced by replacing WBT with DBT.

e. Statistical significance test

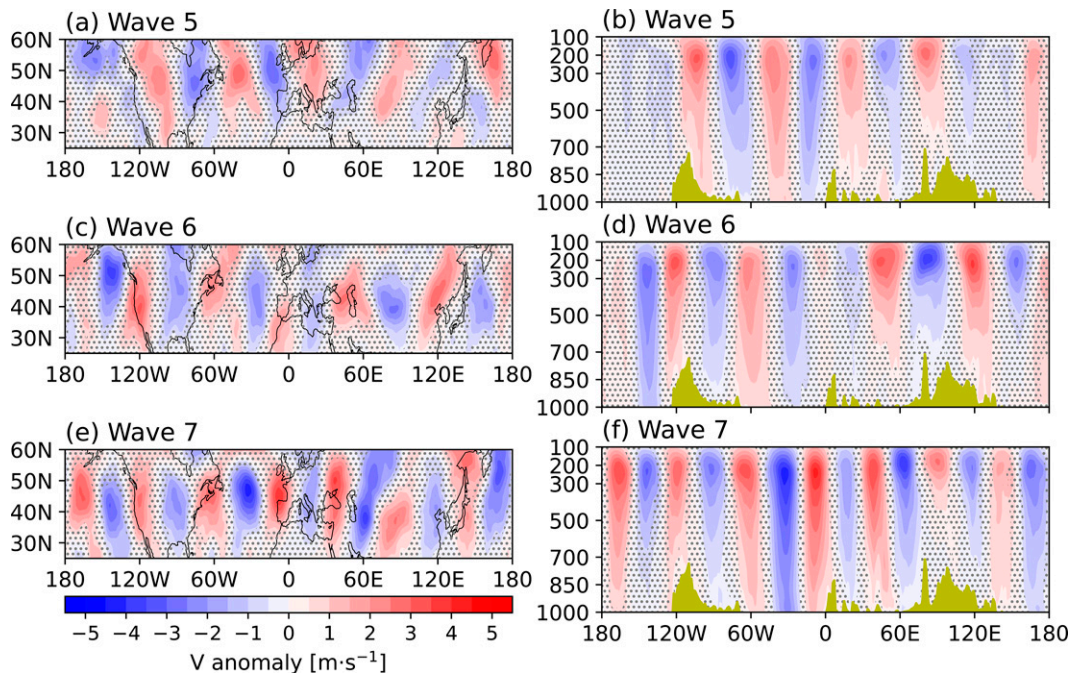Since the distributions of some variables may not follow Gaussian form, we apply a Monte Carlo approach to evaluate

FIG. 2. Composite 300-hPa meridional wind anomalies during months of high-amplitude (a) Wave 5, (c) Wave 6, and (e) Wave 7 (unit: m s^{-1}). Vertical cross sections of composite meridional wind anomalies along 45°N during months of high-amplitude (b) Wave 5, (d) Wave 6, and (f) Wave 7 (unit: m s^{-1}). Red shading represents anomalous southerlies while blue shading represents anomalous northerlies. Gray stippling indicates areas where anomalies are *not* statistically significant based on Monte Carlo test and a control for the false discovery rate. The olive shading in (b), (d), and (f) masks the terrain along 45°N.

statistical significance of composite analysis. When calculating the statistical significance of the anomaly during months of high-amplitude waves, we randomly select N months from 1979 to 2020 JJA, where N corresponds to the number of high-amplitude months for each wavenumber. Then, a composite is calculated by compositing a specific variable in the selected N months. This process is repeated 1000 times to obtain an empirical distribution, based on which the $p < 0.1$ significance level is determined at each grid point. When multiple significance tests are conducted in producing the composite map, we follow Wilks (2016) to adjust the p value by controlling the false discovery rate (FDR) of spatially correlated data ($\alpha_{FDR} = 0.2$). An FDR control of 0.2 is, for non-spatially correlated data, associated with the expectation that 20% of the grid points identified as significant are actually consistent with the null hypothesis, although the test can be conservative for spatially correlated data (Wilks 2016).

Besides, the Monte Carlo approach is also used to assess the statistical significance of the difference between the MEX distribution of months with high-amplitude Wave 5–7 and that of the remaining months not characterized by amplified Wave 5–7, with regard to the mean, standard deviation, and cumulative probability of positive MEX. We randomly select N and M months from 1979 to 2020 JJA, where N corresponds to the number of months with high-amplitude Wave 5–7 ($N = 50$) and M corresponds to the number of the rest months ($M = 76$). Then, the differences in the mean, standard

deviation, and cumulative probability metric of MEX between the N and M selected months are calculated. We repeat this process 5000 times to generate empirical distributions of the differences in specific statistics between the two groups of months (Fig. S2). By comparing the observed differences of the three statistics with the corresponding empirical distributions, we regard the observed differences as statistically significant at a 90% confidence level when they are either above the 95th percentile or below the 5th percentile of the empirical distributions.

3. Three-dimensional structures of amplified Wave 5–7

The three-dimensional structures of amplified Wave 5–7 are examined through composite horizontal sections at 300 hPa and vertical sections along 45°N of meridional wind anomalies during months of high-amplitude Wave 5–7 identified in section 2b (Fig. 2). For each wavenumber, a circumglobal wave pattern in the upper troposphere is clearly observed, indicating that the months of high-amplitude waves capture the corresponding wavenumbers well. Horizontally, the wave trains are zonally oriented and meridionally confined, with maximum anomalies almost in the latitude zone of 30°–60°N. An anomalous southerly center and an anomalous northerly center constitute an anticyclonic or cyclonic anomaly, in other words, ridge or trough. The wavelike structures of Wave 5–7 have a good correspondence with Rossby wave patterns
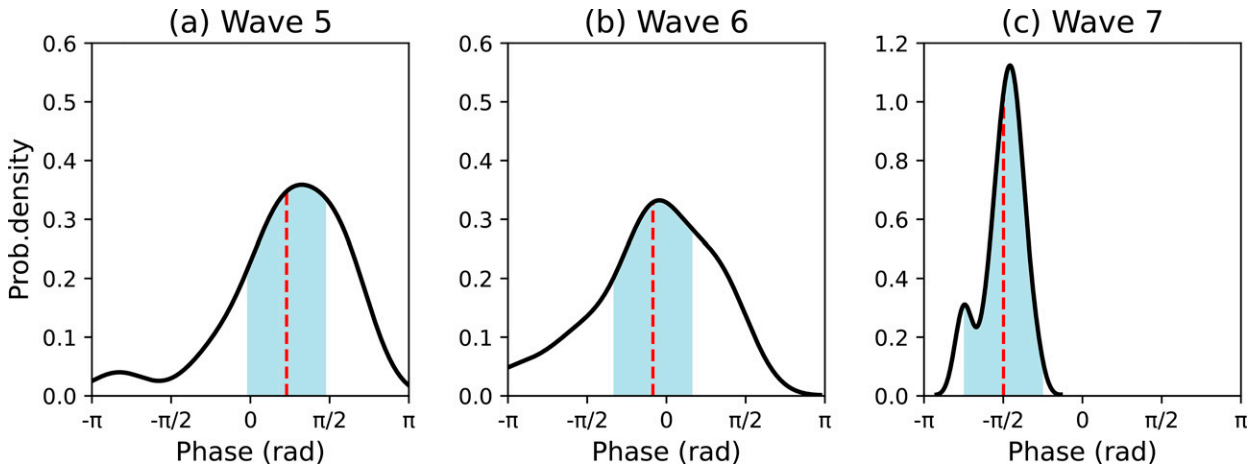
FIG. 3. Probability densities of the phase positions during months of high-amplitude (a) Wave 5, (b) Wave 6, and (c) Wave 7. The range ±π/4 around the peak is shown in light blue. The phases of composite waves are marked with a red dashed line.

depicted in previous studies, even though wave events are selected by different approaches (Kornhuber et al. 2017; Wolf et al. 2018; Kornhuber et al. 2020). Vertically, amplified Wave 5–7 are nearly barotropic and slightly tilt westward with height, consistent with previous studies (Branstator 2002; Wang et al. 2010). The barotropic structures indicate that the wave amplification we detected from the upper-tropospheric circulation can penetrate to the lower troposphere, thus influencing near-surface anomalies and weather extremes.

To ensure that composite wave phases can represent the majority phases of individual months, we examined whether the associated southerly or northerly centers in individual months reoccur over a confined longitudinal range. For this purpose, we quantify the "phase-lock" behavior (Kornhuber et al. 2020) over the latitudinal band 30°–60°N by creating probability density distributions of the phase position of waves in three wavenumbers during high-amplitude months (Fig. 3). For all of three wavenumbers, the distributions exhibit a roughly symmetric single peak, indicating that the associated southerly or northerly centers reoccur over a confined longitudinal range: their phases have a tendency to be "locked." In addition, the phases of composite waves are close to the peak. These results give us confidence about that the composite patterns generally captured the common features of the southerly or northerly centers of the waves in the high-amplitude months, although the patterns may not perfectly match.

4. Relationships between amplified Wave 5–7 and WBT extremes

Is the surface WBT more extreme during months of high-amplitude QSWs? To find the answer, we first compare the probability density distribution of MEX over land during months characterized by high-amplitude Wave 5–7 and that during the remaining months (Fig. 4). The mean and standard deviation of MEX are 0.15 and 0.87 during high-amplitude Wave 5–7 months, whereas they are −0.10 and 1.06 during the months without

amplified Wave 5–7 patterns. The MEX distribution during months of high-amplitude Wave 5–7 has a significantly larger mean value but a significantly smaller standard deviation than that during the remaining months at a 90% confidence level (Figs. S2a,b), which indicates that the overall distribution of MEX shifts toward larger values but is less variable during high-amplitude QSW months. In addition, the cumulative probability of positive MEX is 0.54 during high-amplitude months, in contrast to 0.43 during the remaining months. This difference in the cumulative probability between the high-amplitude months and the remaining months exceeds the 90% significance level (Fig. S2c), giving us confidence that months with high-amplitude Wave 5–7 are associated with higher probabilities of positive MEX. As positive MEX denotes WBT extremes occurring simultaneously in many
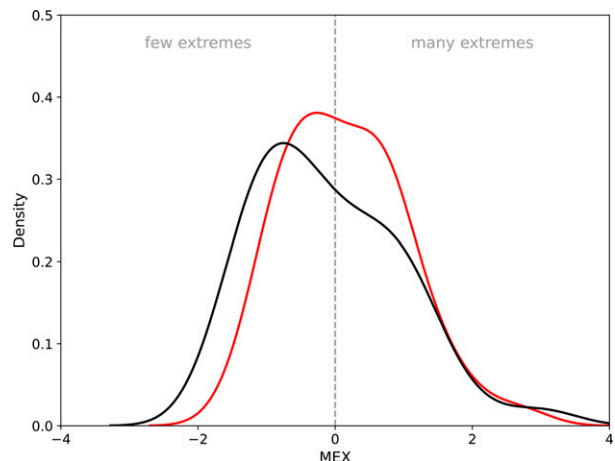

FIG. 4. Probability density of midlatitude extreme (MEX) index over land during months of high-amplitude Wave 5–7 (red) and during the remaining months not characterized by high-amplitude Wave 5–7 (black).
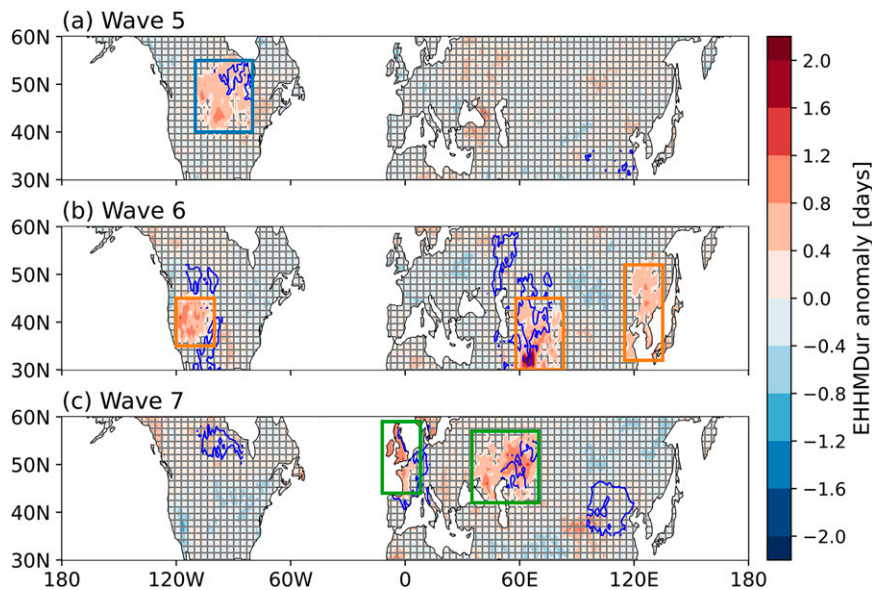
FIG. 5. Composite anomalies of extreme humid heat maximum duration (EHHMDur; shading; units: days) during months of high-amplitude (a) Wave 5, (b) Wave 6, and (c) Wave 7. Red shading represents increased EHHMDur, while blue shading represents decreased EHHMDur. Gray hachures indicate areas where anomalies of EHHMDur are *not* statistically significant. Significantly positive anomalies of EHTMDur are highlighted by blue contours. Rectangles mark the key regions affected by amplified Wave 5 (blue), Wave 6 (orange), and Wave 7 (green).

locations, these results indicate that WBT extremes are more likely to take place simultaneously in multiple locations over land in the months of high-amplitude Wave 5–7, although the largest MEX value occurs during a month without amplified Wave 5–7 patterns.

To examine the spatial characteristics of relationships between amplified Wave 5–7 and WBT extremes, we respectively composite anomalies of extreme humid heat maximum duration (EHHMDur) for each wavenumber during months of high-amplitude Wave 5–7 (Fig. 5). The statistically significant composite anomalies of extreme high temperature maximum duration (EHTMDur) during the corresponding months of high-amplitude Wave 5–7 are overlapped to highlight their differences. The oceans are masked, as we focus on humid heat extremes over land, which pose a direct threat to humans.

We select key regions (marked by rectangles in Fig. 5) based on significantly positive anomalies of EHHMDur. To ensure that the key regions are sufficiently large, only the regions exceeding 10° of longitude–latitude spatial extension (approximately 10 000 km^2) are selected. Generally speaking, most key regions of increased EHHMDur correspond to the regions of anomalous southerlies depicted in Fig. 2. For amplified Wave 5, more prolonged WBT extremes are observed over north-central North America (hereafter referred to as Region-W5: 40°–55°N, 110°–80°W) and most of them are statistically significant based on both the Monte Carlo test and a control for false discovery rate (Fig. 5a). For amplified Wave 6, three key regions are targeted (Fig. 5b). The first is the western

United States (Region1-W6: 35°–45°N, 120°–100°W), where significantly positive anomalies of EHHMDur appear. The second region is south central Asia (Region2-W6: 30°–45°N, 58°–83°E). Significantly increased EHHMDur values are observed over Afghanistan, Kyrgyzstan, Pakistan, Tajikistan, and Uzbekistan. The third one is eastern Asia, including North China, Northeast China, and the Korean Peninsula (Region3-W6: 32°–52°N, 115°–135°E). For amplified Wave 7, we target two key regions (Fig. 5c). One is western Europe, including Britain, France, and Ireland (Region1-W7: 44°–59°N, 12°W–8°E); the other is the Caspian Sea region (Region2-W7: 42°–57°N, 35°–70°E). Significantly increased EHHMDur is observed over a large area on the north of Caspian Sea.

Then we compare the features of WBT extremes with that of high-temperature extremes. In most key regions, the distributions of WBT extremes related to high-amplitude QSWs reveal discrepancies from those of high-temperature extremes, implying that relationships between high-amplitude QSWs and humid heat extremes may be different from that between high-amplitude QSWs and high-temperature extremes. In Region-W5, significantly increased EHTMDur only appears over the northeastern parts of this region. In Region1-W6 and Region3-W6, there are only very small areas of significantly positive anomalies of EHTMDur compared with that of EHHMDur. In Region2-W7, significantly positive EHHMDur appears to both the northeast and the northwest of the Caspian Sea, while significantly positive EHTMDur is only observed to the northeast of the Caspian Sea. Only in Region2-W6 and Region1-W7 do significantly
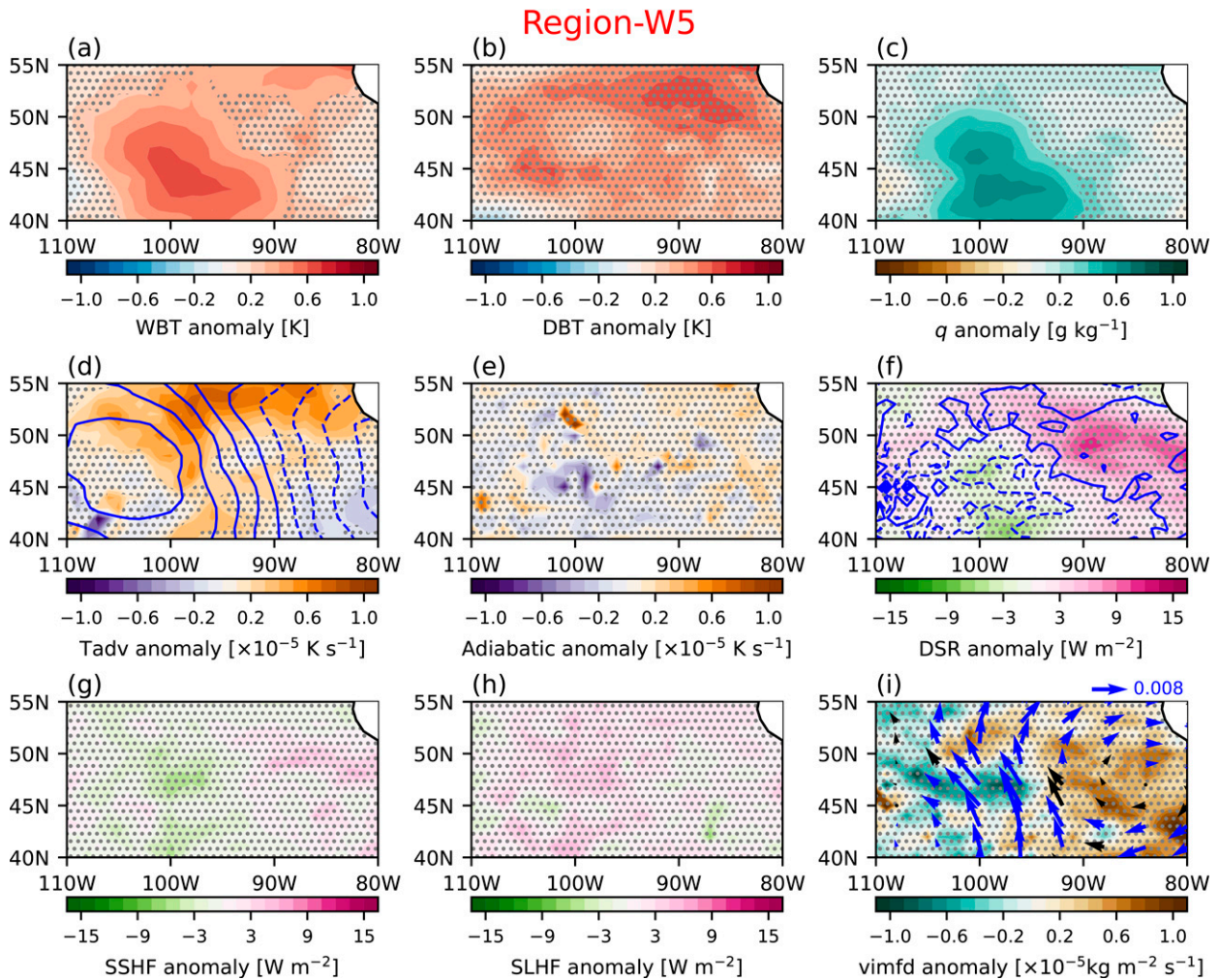
FIG. 6. Composite anomalies of (a) near-surface WBT (unit: K), (b) near-surface DBT (unit: K), (c) near-surface q (unit: g kg^{-1}), (d) 925-hPa temperature advection (Tadv; shading; unit: $\times 10^{-5}$ K s^{-1}) and 300-hPa meridional wind (V; blue contours; contour interval = 0.5 m s^{-1}), (e) 925-hPa adiabatic heating associated with vertical motion (Adiabatic; unit: $\times 10^{-5}$ K s^{-1}), (f) surface downward solar radiation (DSR; shading; unit: W m^{-2}) and 500-hPa vertical velocity at a pressure-based vertical coordinate system (ω; blue contours; contour interval: 0.008 Pa s^{-1}), (g) surface sensible heat flux (SSHF; unit: W m^{-2}), (h) surface latent heat flux (SLHF; unit: W m^{-2}), and (i) 925-hPa moisture flux (mf; vectors; unit: kg kg^{-1} m s^{-1}) and vertical integral of moisture flux divergence (vimfd; shadings; unit: $\times 10^{-5}$ kg m^{-2} s^{-1}) in Region-W5 during months of high-amplitude Wave 5. Areas where anomalies of (a) WBT, (b) DBT, (c) q, (d) Tadv, (e) Adiabatic, (f) DSR, (g) SSHF, (h) SLHF, and (i) vimfd are *not* statistically significant are marked by gray stippling. Blue arrows in (i) indicate statistically significant anomalies of mf. The solid lines in (d) represent anomalous southerlies while the dashed lines represent anomalous northerlies. The solid lines in (f) represent anomalous descending motion, while the dashed lines represent anomalous ascending motion.

positive anomalies of EHHMDur overlap with that of EHTMDur.

5. The physical processes linking amplified Wave 5–7 to WBT extremes

In this section, we investigate the physical processes through which amplified Wave 5–7 drive WBT extremes in these key regions. The composite patterns of WBT anomalies during high-amplitude QSWs generally resemble the composite patterns of EHHMDur anomalies in all key regions (Figs. 6–8). This indicates that the WBT anomalies related to amplified

Wave 5–7 may provide favorable conditions for the persistence of WBT extremes. As WBT is obtained from a combination of temperature and humidity, the anomalies of WBT may result from the anomalies of either or both of DBT and q. Then dynamic factors that may contribute to the anomalies of DBT or q are examined. Generally speaking, near-surface DBT can be influenced by multiple dynamic factors, such as horizontal temperature advection, adiabatic process associated with vertical motion and static stability, and diabatic heating (including radiation, latent heat, and sensible heat). Dynamic contributors to near-surface humidity include moisture transport, and latent heat flux related to evaporation and condensation.
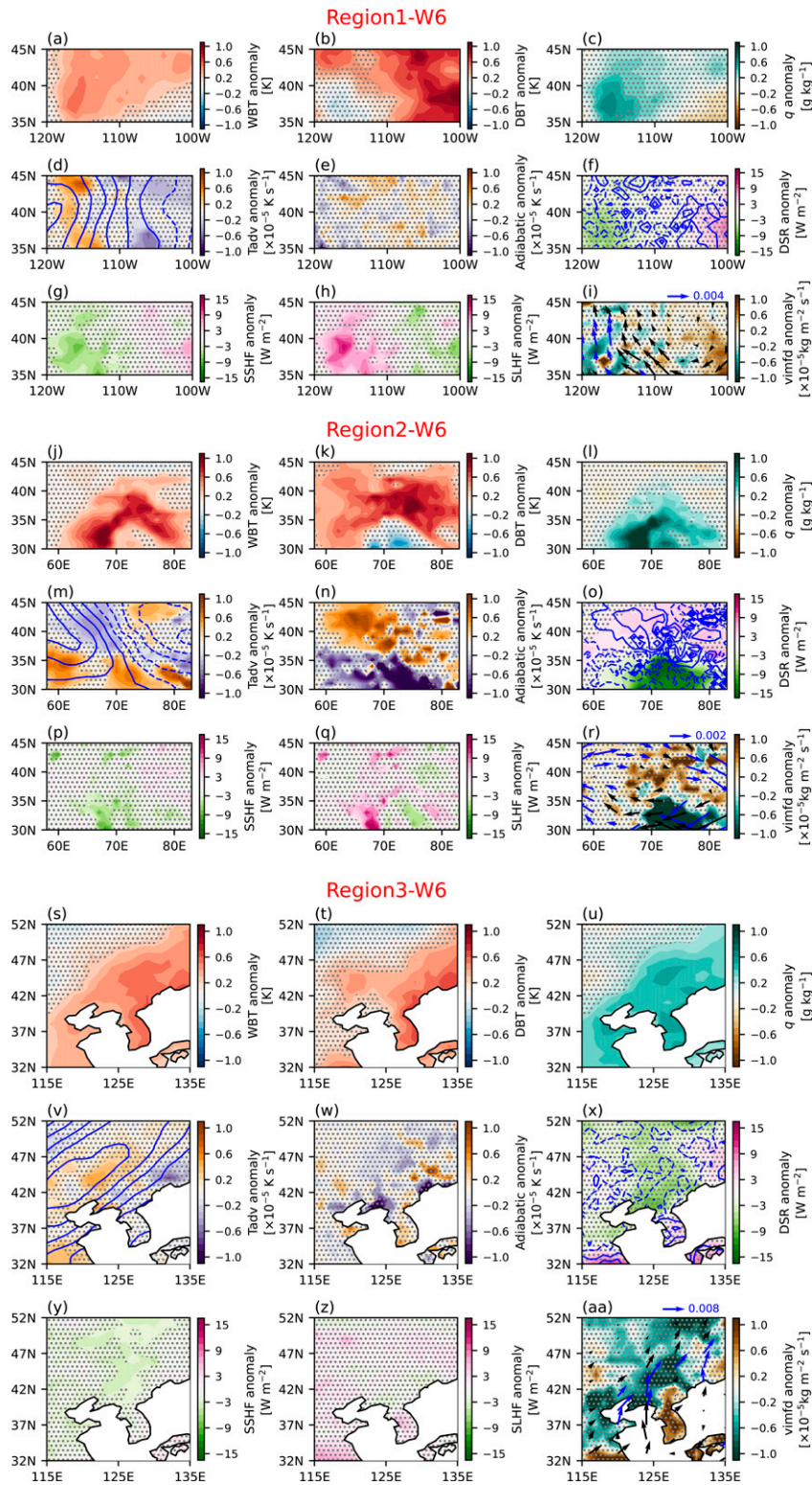
FIG. 7. As in Fig. 6, but for (d) 700-hPa temperature advection, (e) 700-hPa adiabatic heating, and (i) 700-hPa moisture flux in (a)–(i) Region1-W6; (m) 500-hPa temperature advection, (n) 500-hPa adiabatic heating, and (r) 500-hPa moisture flux in (j)–(r) Region2-W6; and (s)–(aa) Region3-W6 during months of high-amplitude Wave 6.
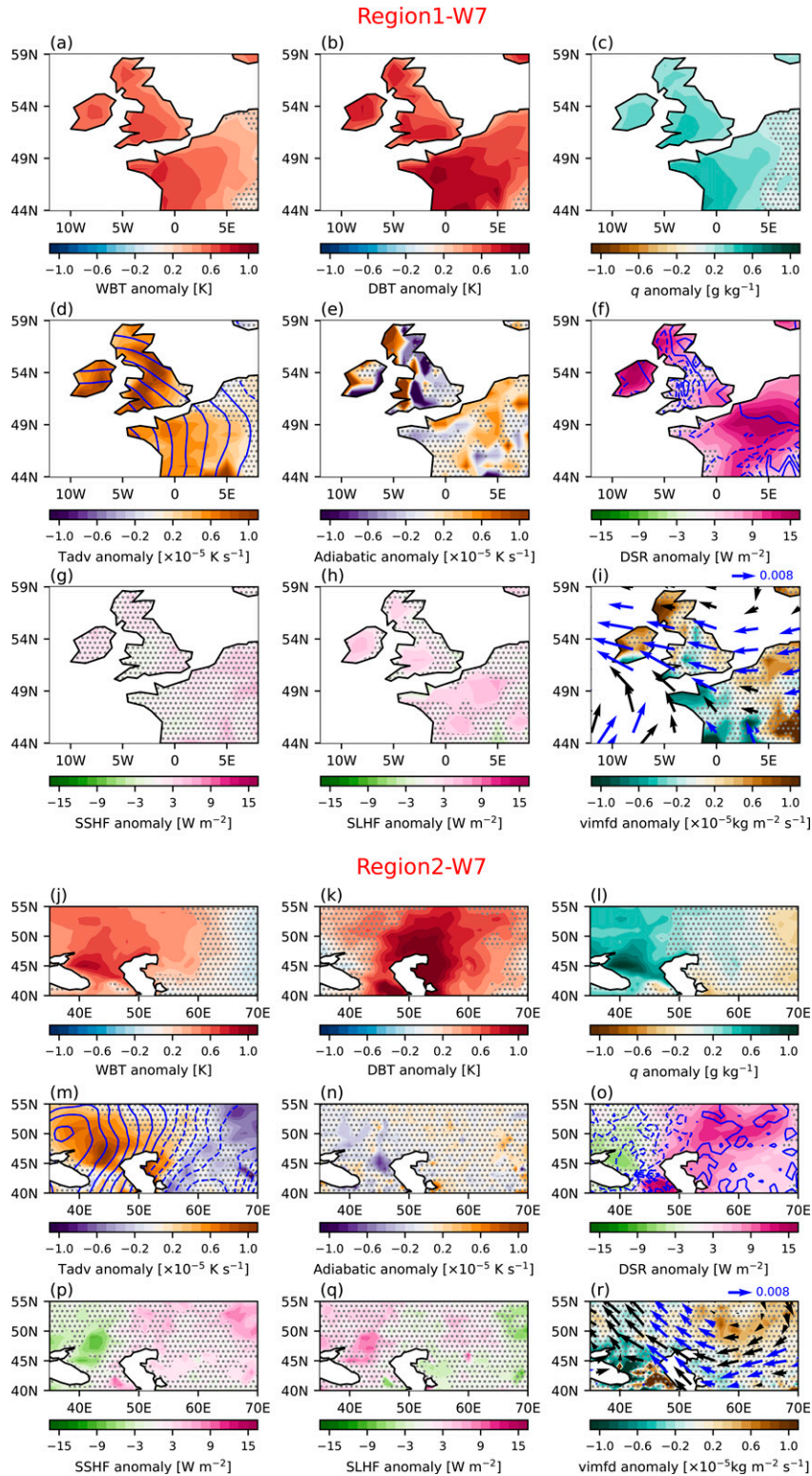
FIG. 8. As in Fig. 6, but for (a)–(i) Region1-W7 and (j)–(r) Region2-W7 during months of high-amplitude Wave 7.

Therefore, we examine variables related to amplified Wave 5–7 for each key region, that is, anomalies of near-surface DBT and q, horizontal temperature advection, adiabatic heating, surface downward solar radiation, 500-hPa vertical velocity, surface sensible/latent heat fluxes, moisture fluxes, and vertical integral of moisture flux divergence. To examine the horizontal temperature advection, adiabatic heating, and moisture flux at a pressure level near the surface, we selected the pressure level according to the elevation of the region: 925 hPa for Region-W5, Region3-W6, Region1-W7, and Region2-W7, 700 hPa for Region1-W6, and 500 hPa for Region2-W6 (Fig. S3).

In Region-W5, significantly positive WBT anomalies are present over the central United States, where significantly positive q anomalies but insignificantly positive DBT anomalies are observed (Figs. 6a–c). This indicates that the anomalously positive WBT over this area is largely contributed by the anomalously positive q, which is derived from significantly anomalous moisture flux from the Gulf of Mexico and intensified moisture flux convergence over the central United States (Fig. 6i). In addition, the significantly positive WBT anomalies observed over the central Canada are consistent with significantly positive anomalies of temperature advection, manifesting the contributions from increased warm advection associated with anomalous southerlies (Fig. 6d).

In Region1-W6, significantly positive WBT anomalies nearly cover the whole region, but the dominant contributors to WBT anomalies are different between the western and eastern part (Figs. 7a–c). In the western area, significantly positive anomalies of q are observed coinciding with intensified moisture flux induced by anomalous southerlies from the tropical Pacific, and positive anomalies of latent heat flux from the surface (Figs. 7h,i). The increased latent heat flux may result from the positive anomalies of precipitation due to anomalous ascending motions increase soil moisture and further promote positive evapotranspiration (Fig. S4a). Over the eastern part, there are significantly positive anomalies of DBT, which probably results from positive anomalies of sensible heat flux from the surface, although only a small area is statistically significant (Fig. 7g). This anomalously positive sensible heat flux may be promoted by increase downward solar radiation due to the descending motion at a ridge of Wave 6 (Fig. 7f).

Region2-W6 is a special case due to its complex terrain, which involves the world's highest mountain range, the Himalayas (Fig. S3). Over the Indo-Gangetic Plain, significantly positive WBT anomalies are observed accompanied by significantly positive q anomalies but significantly negative DBT anomalies (Figs. 7j–l). This indicates that the anomalously positive WBT over this area is mainly contributed by anomalously positive q. The anomalous southerlies and northerlies related to Wave 6 constitute an anomalous high pressure over the entire region. The southeasterlies along the high pressure south edge transport humid air toward the Indo-Gangetic Plain, where strong moisture flux convergence occurs, leading to significantly positive q anomalies (Fig. 7r). Over the Hindu Kush, Sulaiman Range, and Himalayas, significantly positive anomalies of WBT coincide with significantly positive anomalies of DBT and q, indicating that contributions from both variables are important for the anomalously positive WBT.

Over this area, the anomalous descending motion under the anomalous high increases downward solar radiation and adiabatic heating, inducing anomalously positive DBT (Figs. 7n,o). Significantly positive anomalies of surface latent heat flux are observed over the Sulaiman Range, where precipitation increases significantly (Fig. 7q; see also Fig. S4b). This indicates an indirect contribution of increased precipitation over the windward slope to latent heat fluxes, which further increase the near-surface humidity.

As for Region3-W6, significantly positive anomalies of WBT depict similar spatial patterns with significantly positive anomalies of both DBT and q, manifesting both their contributions (Figs. 7s–u). The anomalously positive DBT mainly results from increased warm advection related to anomalous southerlies (Fig. 7v). Meanwhile, the anomalous southerlies transport moisture from the Yellow Sea, contributing to anomalously positive q over main land of northeastern Asia (Fig. 7aa).

In Region1-W7, the significantly positive WBT anomalies coincide with positive DBT anomalies and positive q anomalies, indicating that the WBT anomalies over this region are contributed by positive anomalies of both temperature and moisture (Figs. 8a–c). Over this region, the positive DBT anomalies may be induced by positive temperature advection anomalies through the anomalous southerlies from the Bay of Biscay (Fig. 8d). Meanwhile, anomalous descending motion promotes downward solar radiation and adiabatic heating, thus increasing the surface air temperature (Figs. 8e,f). In addition, there is intensified moisture flux from the Bay of Biscay and the Baltic Sea toward western Europe, providing sufficient water vapor for anomalously positive q (Fig. 8i). At the same time, significantly positive anomalies of latent heat fluxes from the surface to atmosphere are observed, perhaps contributing to the increase in q (Fig. 8h).

For Region2-W7, significantly positive WBT anomalies are observed to the northwest of the Caspian Sea, where there are significantly positive q anomalies, while positive DBT anomalies only around the northwest coast of the Caspian Sea (Figs. 8j–l). This suggests the anomalously positive WBT is largely contributed by anomalously positive q, which may result from intensified northwestward moisture flux from the Caspian Sea and surface latent heat flux to the northwest of the Caspian Sea (Figs. 8q,r). The significantly positive anomalies of surface latent heat flux may be induced by positive anomalies of precipitation (Fig. S4d) due to anomalous ascending motion and moisture flux convergence (Figs. 8o,r). In addition, the anomalously positive WBT over the areas to the north and northeast of the Caspian Sea is concomitant with significantly positive DBT anomalies, revealing the dominant contribution of DBT to the positive WBT anomalies. There is significantly increased downward solar radiation associated with anomalous descending motion, which results in the emergence of anomalously positive DBT (Fig. 8o).

6. Conclusions and discussion

In this study, the linkages between high-amplitude QSWs in multiple zonal wavenumbers and humid heat extremes in

the NH midlatitudes are investigated based on the reanalysis dataset ERA5. With a focus on zonal wavenumbers 5–7, we selected 18, 17, and 15 months of high-amplitude Wave 5, 6, and 7, and composited to identify their features, respectively. Over the NH midlatitudes, amplified Wave 5, 6, and 7 are all characterized by clear circumglobal wave patterns with corresponding wavenumber in the horizontal direction, and nearly barotropic in the vertical direction. Amplified Wave 5–7 with diverse spatial patterns imply various impacts on near-surface weather and extremes in different regions.

Through composite analyses based on selected months for each wavenumber, it is found that most regions of more prolonged WBT extremes generally correspond to the regions of anomalous southerlies (Fig. 5). In addition, we have identified some key regions where significantly prolonged WBT extremes are related to high-amplitude QSWs: north-central North America for amplified Wave 5; the western United States, south-central Asia, and eastern Asia for amplified Wave 6; and western Europe and the Caspian Sea region for amplified Wave 7. In these selected regions, there are increases in the persistence of WBT extremes, some of which show very different features from that of DBT extremes, likely manifesting different relationships between amplified QSWs and humid heat extremes from that between QSWs and high-temperature extremes.

The physical processes how amplified Wave 5–7 link WBT extremes in each key region mentioned above are explored in detail. During months of high-amplitude QSWs, the anomalously prolonged WBT extremes coincide with positive WBT anomalies. This indicates that high-amplitude QSWs make the monthly WBT higher than normal, providing favorable conditions for persistence of WBT extremes (Figs. 6a, 7a,j,s, and 8a,j). Positive anomalies of monthly WBT during months of high-amplitude QSWs are contributed from positive anomalies of q and DBT mainly from five pathways, listed as follows: 1) Anomalous horizontal winds related to amplified Wave 5–7 increase the near-surface humidity by enhancing moisture transport and moisture flux convergence. Regions influenced by this pathway include the central United States for amplified Wave 5; the western United States, the Indo-Gangetic Plain to the south of the Himalayas, and northeastern China for amplified Wave 6; and the British Isles, France, and the area northwest of the Caspian Sea for amplified Wave 7. 2) Increased warm advection induced by anomalous southerlies of the amplified QSWs brings warm and moist air, making the WBT higher than normal. Regions influenced by this pathway include central Canada for amplified Wave 5; northern and northeastern China for amplified Wave 6; and the British Isles, France, and the area northwest of the Caspian Sea for amplified Wave 7. 3) Anomalous descending motion related to amplified QSWs leads to increased downward solar radiation heating the surface over regions including Hindu Kush and the Himalayas for amplified Wave 6, and the British Isles, France, and the area northeast of the Caspian Sea for amplified Wave 7. 4) Adiabatic heating associated with descending motion makes contributions over regions involving the Hindu Kush and Himalayas for amplified Wave 6 as well as France for amplified Wave 7. 5) Increased

latent heat fluxes from surface to atmosphere contribute to anomalously positive q over the western United States and the Sulaiman Range for amplified Wave 6 and the British Isles, France, and the area northwest of the Caspian Sea for amplified Wave 7.

Our results demonstrate a close relationship between amplified QSWs and humid heat extremes. We identify the key regions where humid heat extremes closely related to amplified QSWs, some of which cannot be elucidated when analyzing dry-bulb temperature alone. Furthermore, it is worth noting that these identified humid heat extremes occurred concurrently in distant regions of the midlatitudes, potentially amplifying the negative impacts on societies in today's interconnected world. These findings may provide important information on the risks of heat stress for local planning.

In the context of climate change, the projected response of QSWs' amplitude varies across different zonal wavenumbers (Wills et al. 2019). Our study investigates QSWs in different zonal wavenumbers independently, and reveals the linkages between the amplified QSWs of each wavenumber and humid heat extremes. Yet the couplings among different zonal wavenumbers have not been considered. If amplification of QSWs in multiple wavenumbers occurs simultaneously, the risks of humid heat extremes may be raised in the locations affected by all.

REFERENCES

Branstator, G., 2002: Circumglobal teleconnections, the jet stream waveguide, and the North Atlantic Oscillation. *J. Climate*, **15**, 1893–1910, https://doi.org/10.1175/1520-0442(2002)015<1893:CTTJSW>2.0.CO;2.

Coumou, D., and S. Rahmstorf, 2012: A decade of weather extremes. *Nat. Climate Change*, **2**, 491–496, https://doi.org/10.1038/nclimate1452.

——, A. Robinson, and S. Rahmstorf, 2013: Global increase in record-breaking monthly-mean temperatures. *Climatic Change*, **118**, 771–782, https://doi.org/10.1007/s10584-012-0668-1.

——, V. Petoukhov, S. Rahmstorf, S. Petri, and H. J. Schellnhuber, 2014: Quasi-resonant circulation regimes and hemispheric

synchronization of extreme weather in boreal summer. *Proc. Natl. Acad. Sci. USA*, **111**, 12 331–12 336, https://doi.org/10.1073/pnas.1412797111.

——, K. Kornhuber, J. Lehmann, and V. Petoukhov, 2017: Weakened flow, persistent circulation, and prolonged weather extremes in boreal summer. *Climate Extremes: Patterns and Mechanisms*, S.-Y. S. Wang et al., Eds., John Wiley & Sons, Inc., 61–73.

Dosio, A., L. Mentaschi, E. M. Fischer, and K. Wyser, 2018: Extreme heat waves under 1.5°C and 2°C global warming. *Environ. Res. Lett.*, **13**, 054006, https://doi.org/10.1088/1748-9326/aab827.

Dunne, J. P., R. J. Stouffer, and J. G. John, 2013: Reductions in labour capacity from heat stress under climate warming. *Nat. Climate Change*, **3**, 563–566, https://doi.org/10.1038/nclimate1827.

Fischer, E. M., S. Sippel, and R. Knutti, 2021: Increasing probability of record-shattering climate extremes. *Nat. Climate Change*, **11**, 689–695, https://doi.org/10.1038/s41558-021-01092-9.

Gampe, D., J. Zscheischler, M. Reichstein, M. O'Sullivan, W. K. Smith, S. Sitch, and W. Buermann, 2021: Increasing impact of warm droughts on northern ecosystem productivity over recent decades. *Nat. Climate Change*, **11**, 772–779, https://doi.org/10.1038/s41558-021-01112-8.

Hersbach, H., and Coauthors, 2020: The ERA5 global reanalysis. *Quart. J. Roy. Meteor. Soc.*, **146**, 1999–2049, https://doi.org/10.1002/qj.3803.

Horton, R. M., J. S. Mankin, C. Lesk, E. Coffel, and C. Raymond, 2016: A review of recent advances in research on extreme heat events. *Curr. Climate Change Rep.*, **2**, 242–259, https://doi.org/10.1007/s40641-016-0042-x.

Kornhuber, K., V. Petoukhov, S. Petri, S. Rahmstorf, and D. Coumou, 2017: Evidence for wave resonance as a key mechanism for generating high-amplitude quasi-stationary waves in boreal summer. *Climate Dyn.*, **49**, 1961–1979, https://doi.org/10.1007/s00382-016-3399-6.

——, D. Coumou, E. Vogel, C. Lesk, J. F. Donges, J. Lehmann, and R. M. Horton, 2020: Amplified Rossby waves enhance risk of concurrent heatwaves in major breadbasket regions. *Nat. Climate Change*, **10**, 48–53, https://doi.org/10.1038/s41558-019-0637-z.

Kovats, R. S., and S. Hajat, 2008: Heat stress and public health: A critical review. *Annu. Rev. Public Health*, **29**, 41–55, https://doi.org/10.1146/annurev.publhealth.29.020907.090843.

Lee, M.-H., S. Lee, H.-J. Song, and C.-H. Ho, 2017: The recent increase in the occurrence of a boreal summer teleconnection and its relationship with temperature extremes. *J. Climate*, **30**, 7493–7504, https://doi.org/10.1175/JCLI-D-16-0094.1.

Li, D., J. Yuan, and R. E. Kopp, 2020: Escalating global exposure to compound heat-humidity extremes with warming. *Environ. Res. Lett.*, **15**, 064003, https://doi.org/10.1088/1748-9326/ab7d04.

Luo, F., and Coauthors, 2022: Summertime circumglobal Rossby waves in climate models: Small biases in upper-level circulation create substantial biases in surface imprint. *Wea. Climate Dyn.*, **3**, 905–935, https://doi.org/10.5194/wcd-3-905-2022.

Mann, M. E., S. Rahmstorf, K. Kornhuber, B. A. Steinman, S. K. Miller, S. Petri, and D. Coumou, 2018: Projected changes in persistent extreme summer weather events: The role of quasi-resonant amplification. *Sci. Adv.*, **4**, eaat3272, https://doi.org/10.1126/sciadv.aat3272.

Meehl, G. A., and C. Tebaldi, 2004: More intense, more frequent, and longer lasting heat waves in the 21st century. *Science*, **305**, 994–997, https://doi.org/10.1126/science.1098704.

Mishra, V., A. K. Ambika, A. Asoka, S. Aadhar, J. Buzan, R. Kumar, and M. Huber, 2020: Moist heat stress extremes in India enhanced by irrigation. *Nat. Geosci.*, **13**, 722–728, https://doi.org/10.1038/s41561-020-00650-8.

Monteiro, J. M., and R. Caballero, 2019: Characterization of extreme wet-bulb temperature events in southern Pakistan. *Geophys. Res. Lett.*, **46**, 10 659–10 668, https://doi.org/10.1029/2019GL084711.

Mora, C., and Coauthors, 2017: Global risk of deadly heat. *Nat. Climate Change*, **7**, 501–506, https://doi.org/10.1038/nclimate3322.

Oudin Åström, D., B. Forsberg, K. L. Ebi, and J. Rocklöv, 2013: Attributing mortality from extreme temperatures to climate change in Stockholm, Sweden. *Nat. Climate Change*, **3**, 1050–1054, https://doi.org/10.1038/nclimate2022.

Patz, J. A., D. Campbell-Lendrum, T. Holloway, and J. A. Foley, 2005: Impact of regional climate change on human health. *Nature*, **438**, 310–317, https://doi.org/10.1038/nature04188.

Petoukhov, V., S. Rahmstorf, S. Petri, and H. J. Schellnhuber, 2013: Quasiresonant amplification of planetary waves and recent Northern Hemisphere weather extremes. *Proc. Natl. Acad. Sci. USA*, **110**, 5336–5341, https://doi.org/10.1073/pnas.1222000110.

——, S. Petri, S. Rahmstorf, D. Coumou, K. Kornhuber, and H. J. Schellnhuber, 2016: Role of quasiresonant planetary wave dynamics in recent boreal spring-to-autumn extreme events. *Proc. Natl. Acad. Sci. USA*, **113**, 6862–6867, https://doi.org/10.1073/pnas.1606300113.

Raymond, C., D. Singh, and R. M. Horton, 2017: Spatiotemporal patterns and synoptics of extreme wet-bulb temperature in the contiguous United States. *J. Geophys. Res. Atmos.*, **122**, 13 108–13 124, https://doi.org/10.1002/2017JD027140.

——, and Coauthors, 2020: Understanding and managing connected extreme events. *Nat. Climate Change*, **10**, 611–621, https://doi.org/10.1038/s41558-020-0790-4.

Rogers, C. D. W., M. Ting, C. Li, K. Kornhuber, E. D. Coffel, R. M. Horton, C. Raymond, and D. Singh, 2021: Recent increases in exposure to extreme humid-heat events disproportionately affect populated regions. *Geophys. Res. Lett.*, **48**, e2021GL094183, https://doi.org/10.1029/2021GL094183.

Russo, S., J. Sillmann, and A. Sterl, 2017: Humid heat waves at different warming levels. *Sci. Rep.*, **7**, 7477, https://doi.org/10.1038/s41598-017-07536-7.

Screen, J. A., and I. Simmonds, 2013: Exploring links between Arctic amplification and mid-latitude weather. *Geophys. Res. Lett.*, **40**, 959–964, https://doi.org/10.1002/grl.50174.

——, and ——, 2014: Amplified mid-latitude planetary waves favour particular regional weather extremes. *Nat. Climate Change*, **4**, 704–709, https://doi.org/10.1038/nclimate2271.

Seneviratne, S. I., and Coauthors, 2021: Weather and climate extreme events in a changing climate. *Climate Change 2021: The Physical Science Basis*, V. Masson-Delmotte et al., Eds., Cambridge University Press, 1513–1766.

Shukla, R., S. Gleixner, A. W. Yalew, B. Schauberger, D. Sietz, and C. Gornott, 2021: Dynamic vulnerability of smallholder agricultural systems in the face of climate change for Ethiopia. *Environ. Res. Lett.*, **16**, 044007, https://doi.org/10.1088/1748-9326/abdb5c.

Stadtherr, L., D. Coumou, V. Petoukhov, S. Petri, and S. Rahmstorf, 2016: Record Balkan floods of 2014 linked to planetary wave resonance. *Sci. Adv.*, **2**, e1501428, https://doi.org/10.1126/sciadv.1501428.

Stendel, M., J. Francis, R. White, P. D. Williams, and T. Woollings, 2021: The jet stream and climate change. *Climate Change*,

3rd ed. T. M. Letcher, Ed., Elsevier, 327–357, https://doi.org/10.1016/B978-0-12-821575-3.00015-3.

Wang, J., Y. Chen, S. F. B. Tett, Z. Yan, P. Zhai, J. Feng, and J. Xia, 2020: Anthropogenically-driven increases in the risks of summertime compound hot extremes. *Nat. Commun.*, **11**, 528, https://doi.org/10.1038/s41467-019-14233-8.

Wang, P., L. R. Leung, J. Lu, F. Song, and J. Tang, 2019: Extreme wet-bulb temperatures in China: The significant role of moisture. *J. Geophys. Res. Atmos.*, **124**, 11 944–11 960, https://doi.org/10.1029/2019JD031477.

——, Y. Yang, J. Tang, L. R. Leung, and H. Liao, 2021: Intensified humid heat events under global warming. *Geophys. Res. Lett.*, **48**, e2020GL091462, https://doi.org/10.1029/2020GL091462.

Wang, S.-Y., L. E. Hipps, R. R. Gillies, X. Jiang, and A. L. Moller, 2010: Circumglobal teleconnection and early summer rainfall in the US Intermountain West. *Theor. Appl. Climatol.*, **102**, 245–252, https://doi.org/10.1007/s00704-010-0260-4.

——, R. E. Davies, and R. R. Gillies, 2013: Identification of extreme precipitation threat across midlatitude regions based on short-wave circulations. *J. Geophys. Res. Atmos.*, **118**, 11 059–11 074, https://doi.org/10.1002/jgrd.50841.

Weilnhammer, V., J. Schmid, I. Mittermeier, F. Schreiber, L. Jiang, V. Pastuhovic, C. Herr, and S. Heinze, 2021: Extreme weather events in Europe and their health consequences—A systematic review. *Int. J. Hyg. Environ. Health*, **233**, 113688, https://doi.org/10.1016/j.ijheh.2021.113688.

Wilks, D. S., 2016: "The stippling shows statistically significant grid points": How research results are routinely overstated and overinterpreted, and what to do about it. *Bull. Amer. Meteor. Soc.*, **97**, 2263–2273, https://doi.org/10.1175/BAMS-D-15-00267.1.

Willett, K. M., N. P. Gillett, P. D. Jones, and P. W. Thorne, 2007: Attribution of observed surface humidity changes to human influence. *Nature*, **449**, 710–712, https://doi.org/10.1038/nature06207.

Wills, R. C. J., R. H. White, and X. J. Levine, 2019: Northern Hemisphere stationary waves in a changing climate. *Curr. Climate Change Rep.*, **5**, 372–389, https://doi.org/10.1007/s40641-019-00147-6.

Wolf, G., D. J. Brayshaw, N. P. Klingaman, and A. Czaja, 2018: Quasi-stationary waves and their impact on European weather and extreme events. *Quart. J. Roy. Meteor. Soc.*, **144**, 2431–2448, https://doi.org/10.1002/qj.3310.

Xu, P., L. Wang, and W. Chen, 2019: The British–Baikal Corridor: A teleconnection pattern along the summertime polar front jet over Eurasia. *J. Climate*, **32**, 877–896, https://doi.org/10.1175/JCLI-D-18-0343.1.

——, and Coauthors, 2021: Amplified waveguide teleconnections along the polar front jet favor summer temperature extremes over northern Eurasia. *Geophys. Res. Lett.*, **48**, e2021GL093735, https://doi.org/10.1029/2021GL093735.

Yuan, J., W. Li, and Y. Deng, 2015: Amplified subtropical stationary waves in boreal summer and their implications for regional water extremes. *Environ. Res. Lett.*, **10**, 104009, https://doi.org/10.1088/1748-9326/10/10/104009.

——, ——, R. E. Kopp, and Y. Deng, 2018: Response of subtropical stationary waves and hydrological extremes to climate warming in boreal summer. *J. Climate*, **31**, 10 165–10 180, https://doi.org/10.1175/JCLI-D-17-0401.1.

——, M. L. Stein, and R. E. Kopp, 2020: The evolving distribution of relative humidity conditional upon daily maximum temperature in a warming climate. *J. Geophys. Res. Atmos.*, **125**, e2019JD032100, https://doi.org/10.1029/2019JD032100.

Zhang, Y., I. Held, and S. Fueglistaler, 2021: Projections of tropical heat stress constrained by atmospheric dynamics. *Nat. Geosci.*, **14**, 133–137, https://doi.org/10.1038/s41561-021-00695-3.